nature COMMUNICATIONS

ARTICLE

Received 1 Dec 2012 | Accepted 16 Oct 2013 | Published 15 Nov 2013

DOI: 10.1038/ncomms3783

Superconductivity at the border of electron localization and itinerancy

Rong Yu[1,2,*], Pallab Goswami[2,†,*], Qimiao Si[2], Predrag Nikolic[3] & Jian-Xin Zhu[4]

The superconducting state of iron pnictides and chalcogenides exists at the border of antiferromagnetic order. Consequently, these materials could provide clues about the relationship between magnetism and unconventional superconductivity. One explanation, motivated by the so-called bad metal behaviour of these materials proposes that magnetism and superconductivity develop out of quasi-localized magnetic moments that are generated by strong electron–electron correlations. Another suggests that these phenomena are the result of weakly interacting electron states that lie on nested Fermi surfaces. Here we address the issue by comparing the newly discovered alkaline iron selenide superconductors, which exhibit no Fermi-surface nesting, to their iron pnictide counterparts. We show that the strong-coupling approach leads to similar pairing amplitudes in these materials, despite their different Fermi surfaces. We also find that the pairing amplitudes are largest at the boundary between electronic localization and itinerancy, suggesting that new superconductors might be found in materials with similar characteristics.

[1] Department of Physics, Renmin University of China, Beijing 100872, China. [2] Department of Physics and Astronomy, Rice University, Houston, Texas 77005, USA. [3] School of Physics, Astronomy and Computational Sciences, George Mason University, Fairfax, Virginia 22030, USA. [4] Theoretical Division and Center for Integrated Nanotechnologies, Los Alamos National Laboratory, Los Alamos, New Mexico 87545, USA. * These authors contributed equally to this work. † Present address: National High Magnetic Field Laboratory, Florida State University, Tallahassee, Florida 32310, USA. Correspondence and requests for materials should be addressed to Q.S. (email: qmsi@rice.edu).

Superconductivity often occurs near a magnetic order. This is the case not only in the iron-based compounds[1–3] but also in heavy fermion intermetallics, organic charge-transfer salts and copper oxides. An important question that is central to these diverse classes of unconventional superconductors is whether the mechanism of their superconductivity is in a way analogous to that of conventional superconductors, with spin fluctuations replacing phonons as the glue for electron pairing, or it instead involves novel electronic states that are generated by strong electron correlations[4].

Iron-based superconductors represent a unique setting to elucidate this basic issue: their large materials parameter space provides the opportunity to understand the microscopic physics by comparing the properties across their material families. A major recent development suitable for this important characteristics is the discovery of high-temperature superconductivity in a new family of iron chalcogenides, the alkaline iron selenides $K_{1-x}Fe_{2-y}Se_2$ (ref. 5). Other related iron selenides, with K replaced in part or in entirety by Rb, Cs or Tl behave similarly[6,7]. The key property is that the maximum of the superconducting transition temperature (T_c) observed in the alkaline iron selenides, above 30 K, is similar to that of their 122 iron pnictides counterpart, suggesting a commonality in the underlying mechanism for superconductivity across these systems.

Compared with those of the iron pnictides, the Fermi surfaces in the alkaline iron selenides are very different. Although the former contain both electron and hole pockets, respectively, at the boundary (M) and centre (Γ) of the one-Fe Brillouin zone, only electron pockets are present in the alkaline iron selenides[8–10]. The weak-coupling Fermi-surface-based mechanism will operate very differently in the alkaline iron selenides compared with the iron pnictides[11–13].

Here we demonstrate that, by incorporating the bad metal nature of the normal state, the strong-coupling approach provides the understanding for the comparable pairing strength in the alkaline iron selenides and iron pnictides.

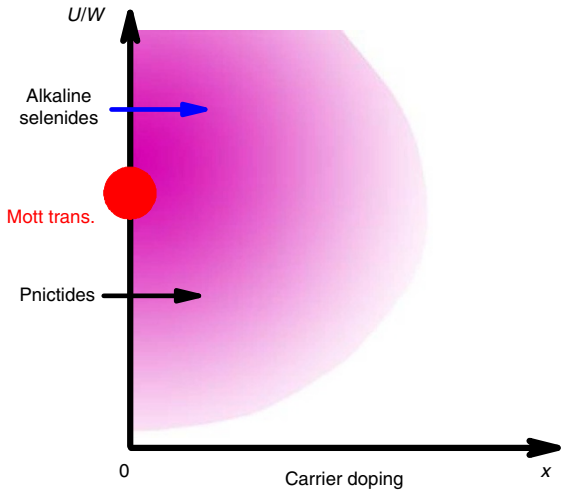

Figure 1 | Schematic phase diagram near a Mott transition. In this zero-temperature phase diagram, the red point located on the U/W axis refers to the point of the Mott transition, whereas the purple shading illustrates the regime that has strong anti-ferromagnetic correlations. The parent compounds of alkaline iron selenides and iron pnictides are located in the vicinity of, albeit on the two sides of, the Mott transition. Superconductivity occurs at non-zero carrier doping, with the optimal doping located in the region indicated by the arrows.

Results

Proximity to Mott transition. We seek for the commonality between the iron chalcogenides and pnictides based on the observation that the parent compound of the alkaline iron selenides are anti-ferromagnetic insulators[6,14]. These insulating selenides contain Fe vacancies that are ordered in the Fe-square lattice, so that the Fe valence is kept at $+2$. Because of their very large ordered moment of about 3.3 μ_B/Fe (refs 15,16), they are naturally considered as Mott insulators, arising through a kinetic energy reduction induced by the ordered vacancies[17,18]. An important question is how U/W, the ratio of a combined onsite Coulomb and Hund's interaction to the electron bandwidth, compares with the Mott-transition threshold, U_c/W. Given that a modest reduction of the kinetic energy from the parent iron pnictides to the parent alkaline iron selenides turns the system from metallic to insulating, we can infer that U/W is larger than but close to U_c/W in the alkaline iron selenides, whereas smaller than but also close to U_c/W in the iron pnictides. Hence, both superconductors arise out of bad metals on the verge of a Mott localization.

This is illustrated in Fig. 1 showing the parent compounds of the alkaline iron selenides and iron pnictides in the vicinity of, albeit on the two sides of, the Mott transition point. Consequently, we use the Mott transition point as anchoring the regime of the phase diagram that has strong anti-ferromagnetic correlations, illustrated by the purple shading in Fig. 1. At the Mott transition point, all the electronic excitations are incoherent. Integrating out the gapped electronic excitations gives rise to a model of localized spins with nearest-neighbour (n.n.) (J_1) and next-nearest-neighbour (n.n.n.) (J_2) interactions on the Fe-square lattice. In the carrier doped regime, a five-band t–J_1–J_2 model ensues[19–21]. More generally, for the iron pnictides, the proximity to the Mott transition has also been supported by the bad metal behaviour of the normal state, as determined by the optical conductivity[3] and other measurements, providing the basis for strong-coupling approaches to superconductivity[19–26].

Multiorbital t–J_1–J_2 approach. We study spin singlet pairings in two such five-band t–J_1–J_2 models, respectively, for the alkaline iron selenides and iron pnictides. The different Fermi surfaces arise from different choices of the tight-binding parameters, which are specified by the kinetic energy part of the model. The five $3d$ orbitals of iron are used to correctly describe the Fermi surfaces; they are denoted by $\alpha = 1,...,5$, which correspond to $3d_{xz}$, $3d_{yz}$, $3d_{x^2-y^2}$, $3d_{xy}$ and $3d_{3z^2-r^2}$ (see Methods). The Fermi surface of $K_{1-x}Fe_{2-y}Se_2$ is shown in Fig. 2a. It comprises electron pockets only, and corresponds to an electron doping of about 15% per Fe; both have been specified in accordance with the angle-resolved photoemission spectroscopy (ARPES) measurements[8–10]. The electron- and hole-like Fermi pockets for the iron pnictides[27], also with $\delta = 15\%$ electron doping, are displayed in Fig. 2b. The xz/yz and xy $3d$ orbitals dominate the electronic states near the Fermi surfaces, as illustrated in Fig. 2c,d. We observe that, at and near zero doping ($\delta = 0$), the ground state will be anti-ferromagnetically ordered (see below). We also note that our study focuses on the couplings in the spin sector as driving the superconductivity, although our general analysis may also have implications for the considerations in the orbital sector[26].

Figure 3a,b demonstrates how superconductivity in the five-band t–J_1–J_2 is magnetically driven by the short-range J_1–J_2 exchange interactions. Shown here, respectively, for $K_{1-x}Fe_{2-y}Se_2$ and iron pnictides, are the zero-temperature phase diagrams in the J_1–J_2 plane, for $0 \leq J_1$ and $J_2 \leq 0.3D$, where D is the

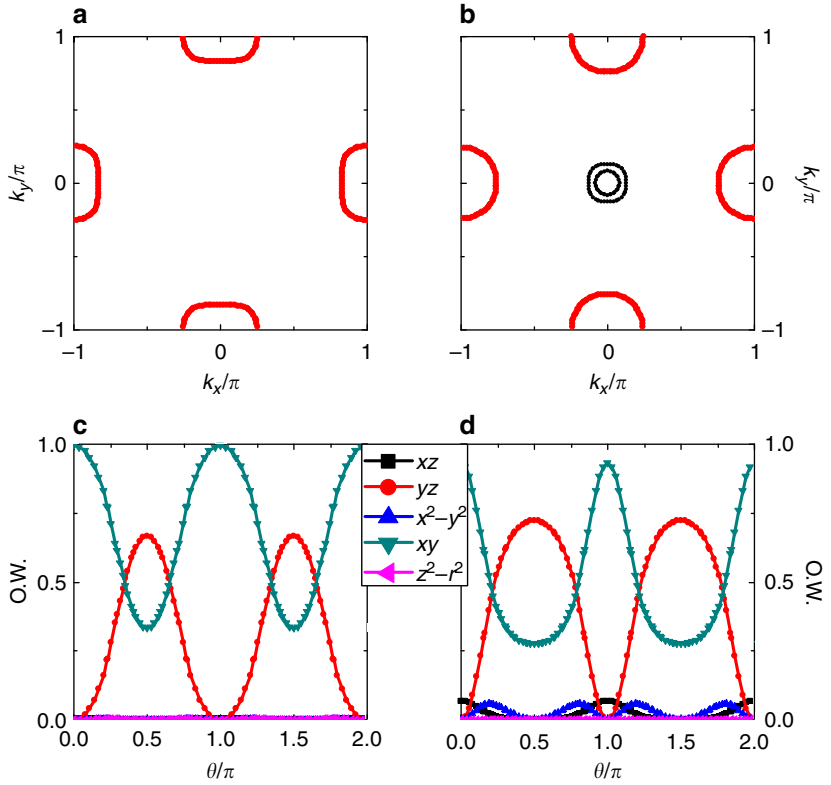

Figure 2 | The contrasting Fermi surfaces of $K_{1-x}Fe_{2-y}Se_2$ and iron pnictides. a and **b**, respectively, show the Fermi surfaces of $K_{1-x}Fe_{2-y}Se_2$ and iron pnictides in the extended Brillouin zone corresponding to one iron per unit cell, as obtained by using a five-orbital tight-binding model described in the Methods section, for electron doping $\delta = 0.15$. There are only electron pockets at the M points $(\pm\pi,0)$ and $(0,\pm\pi)$ for $K_{1-x}Fe_{2-y}Se_2$. For iron pnictides, there are in addition two hole pockets near the Γ point (0,0). (**c,d**) The corresponding orbital weights (O.W.) on the electron pockets centred at $(\pi,0)$ in **a** and **b**. θ is the winding angle of the pocket with respect to its centre. The weights on the electron pocket centred at $(0,\pi)$ can be obtained by interchanging the *xz* and *yz* components and shifting θ by $\pi/2$.

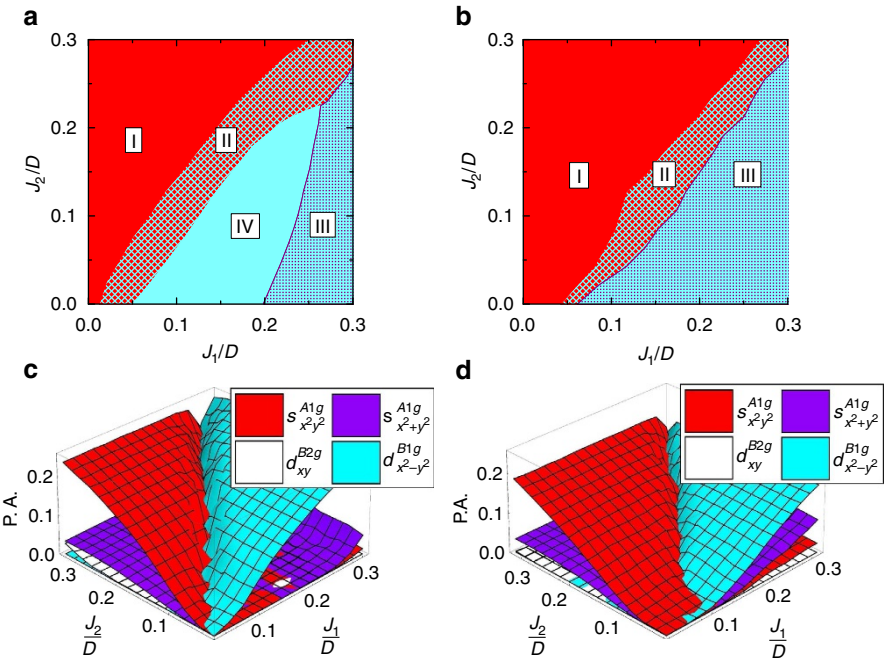

Figure 3 | Phase diagram and pairing amplitudes of $K_{1-x}Fe_{2-y}Se_2$ and iron pnictides. The results presented here are for electron doping $\delta = 0.15$. **a** and **b**, respectively, show the zero-temperature phase diagrams of $K_{1-x}Fe_{2-y}Se_2$ and iron pnictides. Region I corresponds to an A_{1g} state with dominant $s_{x^2y^2}$ channel. Regions II and III mark an $A_{1g}+iB_{1g}$ state with dominant $s_{x^2y^2}$ and $d_{x^2-y^2}$ channels (II), and dominant $s_{x^2+y^2}$ and $d_{x^2-y^2}$ channels (III); the phase locking occurs only at low temperatures. Region IV for $K_{1-x}Fe_{2-y}Se_2$ is a pure B_{1g} state with dominant $d_{x^2-y^2}$ channel. (**c**,**d**)The corresponding pairing amplitudes for the *xy* 3d orbital of $K_{1-x}Fe_{2-y}Se_2$ and iron pnictides.

renormalized bandwidth. For $K_{1-x}Fe_{2-y}Se_2$, the J_2-dominated region I has A_{1g} symmetry, with $s_{x^2y^2}$ ($\cos k_x \cos k_y$) wave being the dominant pairing component. Regions II, III and IV are primarily of the B_{1g} $d_{x^2-y^2}$ ($\cos k_x - \cos k_y$) wave character. The distinction among the three regions reflects the difference in the admixture of a small A_{1g} component at zero (and low) temperatures (see Methods). This is similar to the phase diagram of the pnictides case, where the J_2-dominated region I also is primarily A_{1g} $s_{x^2y^2}$ wave, and regions II and III are primarily B_{1g} $d_{x^2-y^2}$ wave.

To clarify the admixture of the different pairing components, we show the evolution of the amplitudes of these components, projected onto the $3d_{xy}$ orbital, in Fig. 3c,d. Comparing the two figures clearly shows that, for the alkaline iron selenides, the dominant pairing amplitudes in the $s_{x^2y^2}$ and $d_{x^2-y^2}$ channels are comparable to their counterparts in the iron pnictides. This is further illustrated in Fig. 4a,b, which shows the pairing amplitudes, also projected to the $3d_{xy}$ orbital, versus J_1/D for a fixed $J_2/D = 0.1$. The same conclusion applies to the pairing amplitudes projected to the other $3d$ orbitals, as shown in Fig. 4c,d for the case of $3d_{xz}/3d_{yz}$ orbitals.

Pairing amplitudes in alkaline iron selenides. We therefore reach the conclusion that the pairing amplitudes in models, respectively, for the alkaline iron selenides and iron pnictides are similar for given dimensionless exchange interactions, J_1/D and J_2/D. This is surprising because the alkaline iron selenides lack any hole Fermi pocket and, therefore, do not possess any Fermi-surface nesting. Our result is inherent to the strong-coupling approach; here, although the details of the Fermi surfaces are important, the superconducting pairing does not require coupling between hole and electron Fermi pockets. Instead, the driving force for the pairing lies in the close-neighbour exchange interactions, J_1 and J_2. The presence of electron pockets near the M points of the Brillouin zone is adequate to promote the cos $k_x \cos k_y$ A_{1g} $s_{x^2y^2}$ wave pairing, as well as the $\cos k_x - \cos k_y$ B_{1g} $d_{x^2-y^2}$ wave pairing. For similar ratios of J_1/D and J_2/D, the corresponding pairing amplitude is naturally comparable to that of the iron pnictides, in which both the electron pockets near M and the hole pockets near Γ promote these two pairing components.

Enhancement of pairing amplitudes near Mott transition. The results for both classes of materials (Figs 3c,d and 4) also show that the pairing amplitudes are larger when J_1/D and J_2/D are increased. This conclusion, in turn, leads to a general principle. To see this, we note that the exchange interactions increase as the Mott transition is approached from the insulating side (*cf.*, Fig. 1) because of the reduction of the charge gap. At the same time, the renormalized bandwidth D is reduced as the Mott transition is approached from the metallic side. Correspondingly, at the boundary between electronic localization and delocalization, the ratios J_1/D and J_2/D will be maximized and so will the superconducting pairing amplitudes.

Our results provide the understanding for some key experimental observations. Inelastic neutron-scattering experiments have shown that the exchange interactions in the alkaline iron selenides and iron pnictides have the same order of magnitude[16]. Further, as Fig. 1 illustrates, the alkaline iron selenides and iron pnictides have approximately the same doping concentration and similar degree of proximity to the Mott transition. Therefore, J_1/D and J_2/D are similar in the two materials. This leads to our key conclusion, namely, the two classes of iron-based superconductors have comparable pairing amplitudes and, by extension, comparable T_c.

It is instructive to contrast the situation here with KFe_2As_2. The latter system, with the Fermi surface containing only hole pockets[28], represents another material lacking Fermi-surface nesting. However, it is strongly doped, with a hole doping of 0.5 per Fe. This extreme overdoping in KFe_2As_2 means that the system is far away from the Mott transition-anchoring point discussed here and should, therefore, have considerably reduced

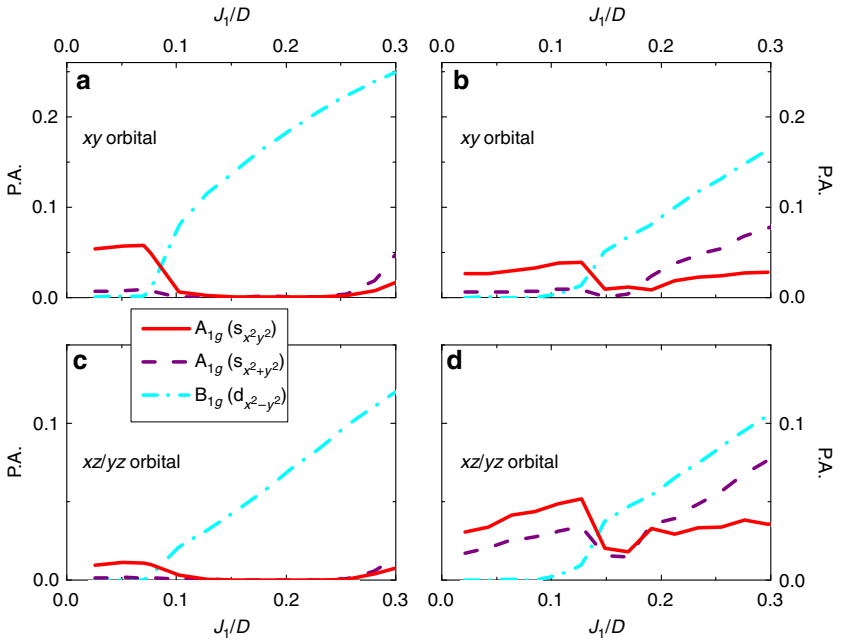

Figure 4 | Pairing amplitudes of $K_{1-x}Fe_{2-y}Se_2$ and iron pnictides for *xy* and *xz/yz* orbitals. (**a,b**) Comparison of the competing dominant pairing amplitudes A_{1g} $s_{x^2y^2}$, A_{1g} $s_{x^2+y^2}$ and B_{1g} $d_{x^2-y^2}$ for the *xy* 3d orbital of $K_{1-x}Fe_{2-y}Se_2$ and iron pnictides, both for electron doping $\delta = 0.15$ and $J_2/D = 0.1$. (**c,d**) The same as **a** and **b** but for the *xz/yz* 3d orbitals. For $K_{1-x}Fe_{2-y}Se_2$ the amplitude for the A_{1g} $s_{x^2+y^2}$ channel is strongly suppressed compared with the pnictides case. Correspondingly, a pure B_{1g} $d_{x^2-y^2}$ state is observed for $K_{1-x}Fe_{2-y}Se_2$ but is absent in iron pnictides.

pairing amplitudes. Experimentally, it indeed has a much smaller T_c of about 3 K.

For the alkaline iron selenides, our results show dominating A_{1g} $s_{x^2y^2}$ and B_{1g} $d_{x^2-y^2}$ wave states in competition. Both have nearly isotropic and nodeless gaps on the electron pockets, and this is consistent with all existing measurements of the superconducting gap. Neutron-scattering experiments have identified a resonance associated with the superconducting state[29]. This is most readily understood in terms of a B_{1g} $d_{x^2-y^2}$ wave pairing[29], although it may also arise from an A_{1g} $s_{x^2y^2}$ channel once the effect of two iron ions per unit cell is taken into account[30]. On the other hand, ARPES experiments have suggested that the superconducting gap is nodeless on the faint electron pocket near the Γ point[30,31]. This appears to favour an A_{1g} $s_{x^2y^2}$ wave pairing[30,31]. Further experiments are needed to settle which of the two possible pairing channels operates in the alkaline iron selenides. For the iron pnictides, the dominance of A_{1g} $s_{x^2y^2}$ state in a large portion of the phase diagram is consistent with the sign-changing $s_{\pm}$ paired state arising in both weak and strong-coupling approaches. Compared with the alkaline iron selenides, an important difference is that the pairing amplitude in the A_{1g} $s_{x^2+y^2}$ channel is sizable (Figs 3,4). This arises because the corresponding form factor, $(\cos k_x + \cos k_y)$, while negligible at the dominant electron Fermi surfaces located near the M points for the alkaline iron selenides, is large near the hole Fermi pockets around the Γ point in the case of the iron pnictides. The relevance of the A_{1g} $s_{x^2+y^2}$ channel is important for understanding a possible strong momentum dependence or even the development of nodes in the superconducting gap; nodes arise on the electron Fermi pockets near the M points when the amplitude of the A_{1g} $s_{x^2+y^2}$ component exceeds a threshold value compared with that of the coexisting A_{1g} $s_{x^2y^2}$ component. Indeed, experimentally, some iron pnictide superconductors show fully gapped behaviour, whereas others display properties that suggest the existence of nodes.

Discussion

The bad metal behaviour near the Mott transition also pertains to the relationship between magnetism and superconductivity in the alkaline iron selenides. For the vacancy-ordered parent insulating system (the so-called 245 phase), it causes the electronic excitations to have a large incoherent component; the latter gives rise to a large spin spectral weight even in the absence of any itinerant carriers, as have been observed by neutron-scattering experiments[15,16].

In superconducting compounds, there is direct evidence for a phase separation[32] between a superconducting component and the parent insulating anti-ferromagnetic part. The superconducting component is free of ordered vacancies[32], suggesting a tetragonal 122 structure as we have used in our model. Our study here focuses on the pairing instabilities in the underlying metallic state of this component while taking advantage of its connection with the Mott-insulating phase in the overall phase diagram[33] discussed in the Supplementary Note 3 (and Supplementary Fig. S5) and evidenced by recent experiments[34–36].

It is worth emphasizing that the physical pathway linking the superconducting phase and 245 Mott-insulating phase involves varying both vacancy order and carrier concentration. Indeed, the existence of the multiple phases of the alkaline iron selenides suggests an overall, extended, parameter space in which the different phases can be connected. This is described in some detail in the Supplementary Note 3 and is in particular illustrated in Supplementary Fig. S5. The details of this physical pathway is a distinct issue that is intriguing and important in its own right[33,34], and other alkaline iron selenides such as $KFe_{1.5}Se_2$, with one vacancy per four iron sites[6,37] (and small carrier doping[34,38]), and $K_{0.5}Fe_{1.75}Se_2$, with one vacancy per eight iron sites[39], may also be placed in this extended phase diagram. For the purpose of the present work, what is particularly pertinent is the clue these multiple phases have provided for the strength of the electron correlations. As described in the introduction and illustrated in Fig. 1, the existence of the Mott-insulating phase in the 245 compound suggests not only that the underlying U/W is larger than U_c/W in the vacancy-ordered alkaline iron selenides but also that U/W is below but close to U_c/W in the iron pnictides. This proximity to the Mott transition allows for the present study on the pairing amplitudes in both classes of iron-based superconductors.

Recently, superconductivity of around 50 K was reported in a single-layer FeSe film grown on $SrTiO_3$ substrate[40]. ARPES measurements[41] indicate that the Fermi surface consists of only electron pockets, similar to that of the alkaline iron selenides. Thus, it is instructive to model the single-layer FeSe film and compare its pairing properties with those of the other iron-based superconductors. We have thus studied the singlet superconductivity in a similar five-orbital t–J_1–J_2 model for the single-layer FeSe film (see Methods), with an electron doping of 0.1 per Fe; we consider the role of the substrate as providing the structure that dopes this amount of electron carriers into the single-layer FeSe[42,43]. The results are shown in Supplementary Figs S4d and S7. The pairing phase diagram of the single-layer FeSe is comparable to those for both alkaline iron selenides and iron pnictides, and so are the overall pairing amplitudes.

By showing that pairing amplitudes are similar for the iron chalcogenides and pnictides in spite of their drastically different Fermi surfaces, our results uncover a universality in the existing and emerging iron-based high-temperature superconductors with very diverse materials and Fermi-surface characteristics. Moreover, our demonstration, that the pairing amplitudes increase with the ratio of the short-range spin exchange energy to the renormalized kinetic energy, reveals an important principle. Namely, superconductivity is optimized at the border between itinerancy and electronic localization. This principle should apply beyond the context of iron pnictides and chalcogenides, and is expected to guide the search for superconductors with even higher transition temperatures.

Methods

Multi-orbital t–J_1–J_2 model. We describe the methods used in our study of the phase diagram for the singlet superconducting pairing of five-orbital t–J_1–J_2 models, described as $H = H_t + H_J$. Here, H_t and H_J, respectively, correspond to the fermion hopping and the J_1–J_2 exchange Hamiltonians.

Two such models are considered. The difference in the fermiology of the alkaline iron selenides and iron pnictides are specified via the kinetic part H_t, and we have chosen the tight-binding parameters by fitting the band dispersions obtained from density functional calculations. The short-range anti-ferromagnetic exchange interactions in H_J drive the singlet pairings. We have chosen the same exchange-coupling constants J_1, J_2 for each orbital, and have performed a mean-field decoupling of the exchange part in the pairing channel. Each orbital contributes four pairing amplitudes $\Delta_{a,\alpha}$, which are, respectively, given by $s_{x^2+y^2,\alpha}$, $d_{x^2-y^2,\alpha}$, $s_{x^2y^2,\alpha}$, $d_{xy,\alpha}$, where $\alpha = 1,...,5$ labels the orbitals; these amplitudes are related to their real-space counterparts, $\Delta_{\mathbf{e},\alpha} = \langle c_{i\alpha\uparrow} c_{i+\mathbf{e}\alpha\downarrow} - c_{i\alpha\downarrow} c_{i+\mathbf{e}\alpha\uparrow} \rangle/2$. We have minimized the free energy to find the self-consistent solution for the 20 pairing amplitudes. We now expound on these in some detail.

Our five-orbital t–J_1–J_2 model arises from an expansion of the five-orbital Hubbard model with respect to the Mott transition point (the 'w-expansion')[20]. The Hamiltonian for the model is given by

$$H = -\sum_{i<j,\alpha,\beta,s} [t_{ij}^{\alpha\beta} c_{i\alpha s}^{\dagger} c_{j\beta s} + h.c.] - \mu \sum_{i,\alpha} n_{i\alpha} + \sum_{\langle ij\rangle,\alpha,\beta} J_1^{\alpha\beta} \left(\vec{S}_{i\alpha} \cdot \vec{S}_{j\beta} - \frac{1}{4} n_{i\alpha} n_{j\beta} \right) + \sum_{\langle\langle ij\rangle\rangle,\alpha,\beta} J_2^{\alpha\beta} \left(\vec{S}_{i\alpha} \cdot \vec{S}_{j\beta} - \frac{1}{4} n_{i\alpha} n_{j\beta} \right) \quad (1)$$

where $c_{i\alpha s}^{\dagger}$ creates an electron at site i, with orbital index α and spin projection s; μ is the chemical potential and $t_{ij}^{\alpha\beta}$ the hopping matrix. The orbital index $\alpha = 1, 2, 3, 4$

and 5 respectively, correspond to five 3*d* orbitals $3d_{xz}$, $3d_{yz}$, $3d_{x^2-y^2}$, $3d_{xy}$ and $3d_{3z^2-r^2}$ of iron. The n.n. ($\langle ij \rangle$) and n.n.n. ($\langle\langle ij \rangle\rangle$) exchange interactions are, respectively, denoted by $J_1^{\alpha\beta}$ and $J_2^{\alpha\beta}$. The spin operator $\vec{S}_{i\alpha}=\frac{1}{2}\sum_{s,s'} c^{\dagger}_{i\alpha s}\vec{\sigma}_{ss'}c_{i\alpha s'}$ and the density operator $n_{i\alpha}=\sum_s c^{\dagger}_{i\alpha s}c_{i\alpha s}$, with $\vec{\sigma}$ representing the Pauli matrices.

For the calculation in these five-orbital models, we have considered the effects of the fermion no double-occupancy constraints as being implicitly accounted for by the reduction of the effective bandwidth *D*. We expect that this treatment does not affect the results qualitatively. We have verified this expectation for a two-orbital model by explicitly keeping track of the occupancy constraints. This is described in some detail in the Supplementary Note 1; Supplementary Methods and Supplementary Fig. S3. As shown there, the phase diagram and pairing amplitudes are insensitive to this when the exchange interactions are measured with respect to the renormalized bandwidth *D*.

In a previous study of a multiorbital t–J_1–J_2 model for iron pnictides[21], it has been demonstrated by three of the present authors that the dominant pairing symmetry is governed by the intraorbital exchange interactions, and the consideration of the orbitally off-diagonal exchange interaction only introduces quantitative modifications of the phase diagram. Therefore, to keep the analysis simple, we will consider the orbitally diagonal exchange couplings $J_1^{\alpha\beta}=J_1\delta_{\alpha\beta}$ and $J_2^{\alpha\beta}=J_2\delta_{\alpha\beta}$. To consider a pure superconducting phase, we will study here the case with the 122 tetragonal symmetry (see Supplementary Note 3 for further discussions).

To describe the fermiology, we use a tetragonal symmetry-preserving tight-binding model, involving all five 3*d* orbitals of iron. In the momentum space, the 5×5 tight-binding matrix, and its eigenvalues will be, respectively, denoted by $\hat{\xi}_k$ and $E_{j,\mathbf{k}}$. The total number of electrons is determined by the chemical potential and the dispersion relations, according to $n=2\sum_{j,\mathbf{k}}\theta(\mu-E_{j,\mathbf{k}})$, and carrier doping $\delta=|n-6|$. The tight-binding parameters are fixed by fitting the band structure obtained from the local density approximation (LDA) calculation. The details of the tight-binding parametrization for iron chalcogenides and the associated band dispersions are discussed below, in the next subsection. For $(K,Tl)_{1-x}Fe_{2-y}Se_2$, the band dispersions correctly produce the electron pockets near the M points, as illustrated in Fig. 2a for $K_{1-x}Fe_{2-y}Se_2$. The electron- and hole-like Fermi pockets obtained from a similar five-orbital tight-binding model of iron pnictides[27] are shown in Fig. 2b to contrast the fermiology of the two materials. The fermiology of $Tl_{1-x}Fe_{2-y}Se_2$ is shown below, in Supplementary Note 2 and Supplementary Figs S1 and S2, which again consists of only electron pockets. We note that ARPES experiments[8–10] have suggested that very weak electron-like pockets may also exist near the Γ points. Unlike their hole counterpart in the iron pnictides, these electron pockets have very small spectral weight and are expected to have at most a secondary role in driving superconductivity.

Details of tight-binding parametrization. For the five orbital, tetragonal symmetry preserving tight-binding model, we adopt the parametrization method of Graser *et al.*[27] We have fitted the LDA band structure with the band dispersion found from the tight-binding model to determine the hopping parameters. For $(K,Tl)_{1-x}Fe_{2-y}Se_2$, we have performed calculations with two different sets of hopping parameters (see Supplementary Tables S1 and S2). These two sets, respectively, were derived from fitting the LDA results for KFe_2Se_2 and $TlFe_2Se_2$; see Supplementary Fig. S1. For iron pnictides, we use the tight-binding parameters of ref. 27. In Figs 2a and 3a, we have shown the electron pockets and pairing phase diagram for the band structure corresponding to $K_{1-x}Fe_{2-y}Se_2$. In Supplementary Fig. S1, we provide the band dispersions for both tight-binding models and also show the electron pockets derived from $Tl_{1-x}Fe_{2-y}Se_2$.

Spin singlet-pairing states. We first consider degenerate pairing states in the absence of kinetic energy. The spin singlet, intraorbital-pairing operators are defined as $\Delta_{\mathbf{e},\alpha}\equiv\Delta_{\mathbf{e},\alpha\alpha}=\langle c_{i\alpha\uparrow}c_{i+\mathbf{e}\alpha\downarrow}-c_{i\alpha\downarrow}c_{i+\mathbf{e}\alpha\uparrow}\rangle/2$, where $\mathbf{e}=\hat{x},\hat{y},\hat{x}\pm\hat{y}$. Two types of pairing states $\Delta_{\hat{x},\alpha}=\pm\Delta_{\hat{y},\alpha}$, respectively, denoted as $s_{x^2+y^2}$ and $d_{x^2-y^2}$ states with momentum space form factors $g_{x^2+y^2,\mathbf{k}}=\cos k_x+\cos k_y$; $g_{x^2-y^2,\mathbf{k}}=\cos k_x-\cos k_y$ arise because of the n.n. exchange interaction, and they are energetically degenerate in the absence of kinetic energy. Similarly, the n.n.n. exchange gives rise to two degenerate pairing states $\Delta_{\hat{x}+\hat{y},\alpha}=\pm\Delta_{\hat{x}-\hat{y},\alpha}$, respectively, denoted as $s_{x^2y^2}$ and d_{xy} states, with momentum space form factors $g_{x^2y^2,\mathbf{k}}=\cos(k_x-k_y)+\cos(k_x+k_y)$, $g_{xy,\mathbf{k}}=\cos(k_x-k_y)-\cos(k_x+k_y)$. A strong magnetic frustration, characterized by $J_1\sim J_2$, leads to an enhanced degeneracy among the four paired states.

The kinetic energy term lifts most of these degeneracies. In the strong frustration regime ($J_1\sim J_2$), it leaves a quasi-degeneracy among a reduced set of pairing states. To study the full problem, we perform a mean-field decoupling[21,44] of the exchange interaction terms. We introduce four complex singlet-pairing amplitudes for each orbital and write the following 5×5 pairing matrix $\Delta_{\mathbf{k}}=\sum_a \mathrm{diag}[\Delta^a_{\mathbf{k},11},\Delta^a_{\mathbf{k},22},\Delta^a_{\mathbf{k},33},\Delta^a_{\mathbf{k},44},\Delta^a_{\mathbf{k},55}]$, where $\Delta^a_{\mathbf{k},\alpha\alpha}=\Delta^a_{\alpha\alpha}g_{a,\mathbf{k}}$ and the index *a* corresponds to $s_{x^2+y^2}$, $d_{x^2-y^2}$, $s_{x^2y^2}$ and d_{xy} symmetries. In the subspace of *xz* and *yz* orbitals, which transform as a doublet under the tetragonal point group operations, there are the following four classes of intraorbital-pairing states for an orbitally diagonal J_1–J_2 model: (i) $A_{1g}:[s^{A_{1g}}_{x^2+y^2}g_{x^2+y^2,\mathbf{k}}+s^{A_{1g}}_{x^2y^2}g_{x^2y^2,\mathbf{k}}]\tau_0+d^{A_{1g}}_{x^2-y^2}g_{x^2-y^2,\mathbf{k}}\tau_z$; (ii) $B_{1g}:d^{B_{1g}}_{x^2-y^2}g_{x^2-y^2,\mathbf{k}}\tau_0+[s^{B_{1g}}_{x^2+y^2}g_{x^2+y^2,\mathbf{k}}+s^{B_{1g}}_{x^2y^2}g_{x^2y^2,\mathbf{k}}]\tau_z$; (iii) $A_{2g}:d^{A_{2g}}_{xy}g_{xy,\mathbf{k}}\tau_z$; and (iv) $B_{2g}:d^{B_{2g}}_{xy}g_{xy,\mathbf{k}}\tau_0$. The eight pairing amplitudes $s^{A_{1g}}_{x^2+y^2}$ and so on are obtained as linear combinations of Δ^a_{11} and Δ^a_{22}, which are in turn linear combinations of $\Delta_{\mathbf{e},11}$ and $\Delta_{\mathbf{e},22}$.

Mixed-symmetry-pairing states breaking time-reversal symmetry. The admixed states II and III of Fig. 3a,b break time-reversal symmetry and have the form $A_{1g}+iB_{1g}$. In regions II and III, the A_{1g} components are, respectively, $s_{x^2y^2}$ $\cos k_x\cos k_y$ and $s_{x^2+y^2}$ $(\cos k_x+\cos k_y)$. In contrast to the pnictides, the pairing phase diagram of 122 chalcogenides has a region IV, which is of purely B_{1g} $d_{x^2-y^2}$ character even at zero temperature. The time-reversal symmetry breaking in region II is because of quasi-degeneracy between $s_{x^2y^2}$ and $d_{x^2-y^2}$ pairings induced by strong magnetic frustration. On the other hand, the quasi-degeneracy between $s_{x^2+y^2}$ and $d_{x^2-y^2}$ pairings in region III arises because of bandwith suppression. These mixed-symmetry-pairing states are expected to be relevant only at sufficiently low temperatures.

Generalizations of the models. The pairing phase diagrams, shown in Fig. 3a,b, have been determined by assuming orbitally diagonal exchange couplings J_1 and J_2. The interorbital exchange couplings do not qualitatively modify the phase diagram. The interorbital couplings introduce some subdominant components to A_{1g} and B_{1g} regions, while leaving the competition between A_{1g} and B_{1g} pairing symmetries intact. For example, an interorbital second neighbour coupling between *xz* and *yz* orbitals gives rise to interorbital $d_{xy}(\sin k_x\sin k_y)$ component, which is a part of A_{1g} pairing. Similarly, we can also consider further neighbour intraorbital exchange couplings. For example, the third neighbour anti-ferromagnetic exchange-coupling J_3 does not change the competing pairing channels; however, it introduces subdominant A_{1g} $(\cos 2k_x+\cos 2k_y)$ and B_{1g} $(\cos 2k_x-\cos 2k_y)$ components. Therefore, the phase diagram obtained from an orbitally diagonal J_1–J_2 model is generic and robust.

We also note that an extended J_1–J_2 model[16,45], with ferromagnetic n.n. coupling, defined on a modulated square lattice, has been used to explain the $\sqrt{5}\times\sqrt{5}$ block spin anti-ferromagnetic order. Although this is believed to reflect the modulation to the exchange interactions that exists only in the presence of ordered vacancies[45,46], it is interesting to consider the effect of a ferromagnetic J_1. The latter will suppress the B_{1g} pairing and increase the A_{1g} region. We stress that the A_{1g}–B_{1g} competition described earlier is the feature of the paramagnetic state, which is devoid of vacancy order and should have an anti-ferromagnetic J_1.

Finally, higher-spin interactions such as a biquadratic term can also be incorporated in the model. These interactions will generate contributions to the free energy that are of higher order in the pairing amplitudes. Therefore, they will not significantly affect the competition among the different pairing channels.

Estimate of the superconducting energy gaps. Our results allow an order-of-magnitude estimate of the pairing energy gaps for the alkaline iron selenides and optimally doped iron pnictides. For both alkaline iron selenides and iron pnictides, the energies of the zone-boundary magnetic excitations are on the order of 200 meV, which imply that the effective exchange interactions are on the order of 20–50 meV[16,47]. This specifies the order of magnitude of the parameters J_1 and J_2 in our model, although they are for individual orbitals. Our calculated values for the pairing amplitudes Δ (Fig. 3c,d) then imply that the corresponding pairing gaps, $\sim 2J\Delta$, appropriately weighted over the different orbitals, will be on the order of 10 meV. This is compatible with what have been inferred from the ARPES and tunnelling measurements[8–10,32].

Pairing for the single-layer FeSe film. We consider the spin singlet pairing of a five-orbital t–J_1–J_2 model for the newly discovered single-layer FeSe film[40]. Recent experiments[40,41] suggest that superconductivity arises from the FeSe layer but not from the FeSe/$SrTiO_3$ interface. Hence, we study, using density functional theory, the electronic structure of a single-layer FeSe without including a substrate. We then use a five-orbital tight-binding parametrization described earlier in the Methods section to fit the density functional theory bandstructure. The best-fitted tight-binding parameters are listed in Supplementary Table S3. Supplementary Figure S6a shows the bandstructure of the tight-binding model with these parameters. We have fixed the Fermi energy so that the electron doping is 0.1 per Fe, which is close to the value of 0.09 per Fe determined by ARPES measurement[41]. As shown in Supplementary Fig. S6b, the calculated Fermi surface comprises electron pockets only, which is consistent with the ARPES results[41]. The overall bandwidth of this model is somewhat larger than that of $K_{1-x}Fe_{2-y}Se_2$, suggesting the electrons are less correlated in the single-layer FeSe than in alkaline iron selenides. This is consistent with the weaker mass renormalization observed in the single-layer FeSe film[41].

Given these tight-binding parameters for the single-layer FeSe, the corresponding five-orbital t–J_1–J_2 model is specified as described earlier in the Methods section. We again consider spin singlet pairing. Supplementary Figure S7 shows the pairing phase diagram and pairing amplitudes in several channels. Both phase diagram and strength of the pairing amplitudes are similar to those of alkaline iron selenides $K_{1-x}Fe_{2-y}Se_2$ and $Tl_{1-x}Fe_{2-y}Se_2$.

References

1. Kamihara, Y., Watanabe, T., Hirano, M. & Hosono, H. Iron-based layered superconductor La[$O_{1-x}F_x$]FeAs ($x = 0.05 - 0.12$) with $T_c = 26$ K. *J. Am. Chem. Soc.* **130,** 3296–3297 (2008).
2. Dai, P., Hu, J. & Dagotto, E. Magnetism and its microscopic origin in iron-based high-temperature superconductors. *Nat. Phys.* **8,** 709–718 (2012).
3. Qazilbash, M. M. *et al.* Electronic correlations in the iron pnictides. *Nat. Phys.* **5,** 647–650 (2009).
4. Anderson, P. W. Is there glue in cuprate superconductors? *Science* **316,** 1705–1707 (2007).
5. Guo, J. *et al.* Superconductivity in the iron selenide $K_xFe_2Se_2$ ($0 \le x \le 1.0$). *Phys. Rev. B* **82,** 180520 (2010).
6. Fang, M. *et al.* Fe-based superconductivity with $T_c = 31$ K bordering an antiferromagnetic insulator in (Tl,K)Fe_xSe_2. *Europhys. Lett.* **94,** 27009 (2011).
7. Sun, L. *et al.* Re-emerging superconductivity at 48 Kelvin in iron chalcogenides. *Nature* **483,** 67–69 (2012).
8. Zhang, Y. *et al.* Nodeless superconducting gap in $A_xFe_2Se_2$ (A = K,Cs) revealed by angle-resolved photoemission spectroscopy. *Nat. Mater.* **10,** 273–277 (2011).
9. Wang, X.-P. *et al.* Strong nodeless pairing on separate electron Fermi surface sheets in (Tl, K)$Fe_{1.78}Se_2$ probed by ARPES. *Europhys. Lett.* **93,** 57001 (2011).
10. Mou, D. *et al.* Distinct Fermi surface topology and nodeless superconducting gap in a ($Tl_{0.58}Rb_{0.42}$)$Fe_{1.72}Se_2$ superconductor. *Phys. Rev. Lett.* **106,** 107001 (2011).
11. Wang, F. *et al.* The electron pairing of $K_xFe_{2-y}Se_2$. *Europhys. Lett.* **93,** 57003 (2011).
12. Maier, T. A., Graser, S., Hirschfeld, P. J. & Scalapino, D. J. *d*-wave pairing from spin fluctuations in the $K_xFe_{2-y}Se_2$ superconductors. *Phys. Rev. B* **83,** 100515 (2011).
13. Khodas, M. & Chubukov, A. V. Interpocket pairing and gap symmetry in Fe-based superconductors with only electron pockets. *Phys. Rev. Lett.* **108,** 247003 (2012).
14. Wang, D. M., He, J. B., Xia, T.-L. & Chen, G. F. Effect of varying iron content on the transport properties of the potassium-intercalated iron selenide $K_xFe_{2-y}Se_2$. *Phys. Rev. B* **83,** 132502 (2011).
15. Bao, W. *et al.* A novel large moment antiferromagnetic order in $K_{0.8}Fe_{1.6}Se_2$ superconductor. *Chin. Phys. Lett.* **28,** 086104 (2011).
16. Wang, M. *et al.* Spin waves and magnetic exchange interactions in insulating $Rb_{0.89}Fe_{1.58}Se_2$. *Nat. Commun.* **2,** 580 (2011).
17. Yu, R., Zhu, J.-X. & Si, Q. Mott transition in modulated lattices and parent insulator of $(K,Tl)_yFe_xSe_2$ superconductors. *Phys. Rev. Lett.* **106,** 186401 (2011).
18. Zhou, Y., Xu, D.-H., Zhang, F.-C. & Chen, W.-Q. Theory for superconductivity in (Tl,K)Fe_xSe_2 as a doped Mott insulator. *Europhys. Lett.* **95,** 17003 (2011).
19. Si, Q. & Abrahams, E. Strong correlations and magnetic frustration in the high T_c iron pnictides. *Phys. Rev. Lett.* **101,** 076401 (2008).
20. Si, Q., Abrahams, E., Dai, J. & Zhu, J.-X. Correlation effects in the iron pnictides. *New. J. Phys.* **11,** 045001 (2009).
21. Goswami, P., Nikolic, P. & Si, Q. Superconductivity in multi-orbital t-J_1-J_2 model and its implications for iron pnictides. *Europhys. Lett.* **91,** 37006 (2010).
22. Haule, K., Shim, J. H. & Kotliar, G. Correlated electronic structure of $LaO_{1-x}F_xFeAs$. *Phys. Rev. Lett.* **100,** 226402 (2008).
23. Seo, K., Bernevig, B. A. & Hu, J. Pairing symmetry in a two-orbital exchange coupling model of oxypnictides. *Phys. Rev. Lett.* **101,** 206404 (2008).
24. Moreo, A., Daghofer, M., Riera, J. A. & Dagotto, E. Properties of a two-orbital model for oxypnictide superconductors: magnetic order, B_{2g} spin-singlet pairing channel, and its nodal structure. *Phys. Rev. B* **79,** 134502 (2009).
25. Berg, E., Kivelson, S. A. & Scalapino, D. J. A twisted ladder: relating the Fe superconductors to the high-T_c cuprates. *New. J. Phys.* **11,** 085007 (2009).
26. Lv, W., Krüger, F. & Phillips, P. Orbital ordering and unfrustrated (π,0) magnetism from degenerate double exchange in the iron pnictides. *Phys. Rev. B* **82,** 045125 (2010).
27. Graser, S., Maier, T. A., Hirschfeld, P. J. & Scalapino, D. J. Near-degeneracy of several pairing channels in multiorbital models for the Fe pnictides. *New. J. Phys.* **11,** 025016 (2009).
28. Sato, T. *et al.* Band structure and Fermi surface of an extremely overdoped iron-based superconductor KFe_2As_2. *Phys. Rev. Lett.* **107,** 177005 (2011).
29. Park, J. T. *et al.* Magnetic resonant mode in the low-energy spin-excitation spectrum of superconducting $Rb_2Fe_4Se_5$ single crystals. *Phys. Rev. Lett.* **107,** 177005 (2011).
30. Xu, M. *et al.* Evidence for an *s*-wave superconducting gap in $K_xFe_{2-y}Se_2$ from angle-resolved photoemission. *Phys. Rev. B* **85,** 220504 (2012).
31. Wang, X.-P. *et al.* Observation of an isotropic superconducting gap at the Brillouin zone center of $Tl_{0.63}K_{0.37}Fe_{1.78}Se_2$. *Europhys. Lett.* **99,** 67001 (2012).
32. Li, W. *et al.* Phase separation and magnetic order in K-doped iron selenide superconductor. *Nat. Phys.* **8,** 126–130 (2012).
33. Yu, R. & Si, Q. Orbital-selective Mott phase in multiorbital models for alkaline iron selenides $K_{1-x}Fe_{2-y}Se_2$. *Phys. Rev. Lett.* **110,** 146402 (2013).
34. Yi, M. *et al.* Observation of temperature-induced crossover to an orbital-selective Mott phase in $A_xFe_{2-y}Se_2$ (A = K, Rb) superconductors. *Phys. Rev. Lett.* **110,** 067003 (2013).
35. Gao, P. *et al.*Pressure-induced insulator-metal transition and the pathway towards superconductivity in alkaline iron selenide compounds. Preprint at http://arXiv.org/abs/1209.1340 (2012).
36. Li, W. *et al.*Orbital-Selective Mottness in $K_xFe_{2-y}Se_2$ Superconductors Revealed by Pump-Probe Spectroscopy. Preprint at http://arxiv.org/abs/1306.5817 (2013).
37. Zhao, J., Cao, H., Bourret-Courchesne, E., Lee, D.-H. & Birgeneau, R. J. Neutron-diffraction measurements of an antiferromagnetic semiconducting phase in the vicinity of the high-temperature superconducting state of $K_xFe_{2-y}Se_2$. *Phys. Rev. Lett.* **109,** 267003 (2012).
38. Chen, F. *et al.* Electronic identification of the parental phases and mesoscopic phase separation of $K_xFe_{2-y}Se_2$ superconductors. *Phys. Rev. X* **1,** 021020 (2011).
39. Cao, C. & Zhang, F.-C. Electronic structure of vacancy-ordered iron-selenide $K_{0.5}Fe_{1.75}Se_2$. *Phys. Rev. B* **87,** 161105 (2013).
40. Wang, Q. Y. *et al.* Interface-induced high-temperature superconductivity in single unit-cell FeSe films on $SrTiO_3$. *Chin. Phys. Lett.* **29,** 037402 (2012).
41. Liu, D. *et al.* Electronic origin of high-temperature superconductivity in single-layer FeSe superconductor. *Nat. Commun.* **3,** 931 (2012).
42. Tan, S. *et al.* Interface-induced superconductivity and strain-dependent spin density waves in FeSe/$SrTiO_3$ thin films. *Nat. Mater.* **12,** 634–640 (2013).
43. He, S. *et al.* Phase diagram and electronic indication of high-temperature superconductivity at 65 K in single-layer FeSe films. *Nat. Mater.* **12,** 605–610 (2013).
44. Kotliar, G. Resonating valence bonds and d-wave superconductivity. *Phys. Rev. B* **37,** 3664–3666 (1988).
45. Yu, R., Goswami, P. & Si, Q. The magnetic phase diagram of an extended $J_1 - J_2$ model on a modulated square lattice and its implications for the antiferromagnetic phase of $K_yFe_xSe_2$. *Phys. Rev. B* **84,** 094451 (2011).
46. Cao, C. & Dai, J. Block spin ground state and three-dimensionality of $(K,Tl)_yFe_{1.6}Se_2$. *Phys. Rev. Lett.* **107,** 056401 (2011).
47. Zhao, J. *et al.* Spin waves and magnetic exchange interactions in $CaFe_2As_2$. *Nat. Phys.* **5,** 555–560 (2009).

Acknowledgements

This work was supported in part by the NSF Grant number DMR-1309531 and the Robert A. Welch Foundation Grant number C-1411 (R.Y., P.G. and Q.S.), the National Science Foundation of China Grant number 11374361 (R.Y.), the NSF Cooperative Agreement No. DMR-0654118, the State of Florida, and the U. S. Department of Energy through the National High Magnetic Field Laboratory (P.G.), the Office of Naval Research Grant N00014-09-1-1025A and the National Institute of Standards and Technology Grant 70NANB7H6138, Am001 (P.N.), and the U.S. DOE under Contract number DE-AC52-06NA25396, the US DOE Office of Basic Energy Sciences and the Center for Integrated Nanotechnologies—a US DOE user facility (J.-X.Z.).

Author contributions

All authors contributed substantially to this work.

Additional information

Supplementary Information accompanies this paper at http://www.nature.com/naturecommunications

Competing financial interests: The authors declare no competing financial interests.

Reprints and permission information is available online at http://npg.nature.com/reprintsandpermissions/

How to cite this article: Yu, R. *et al.* Superconductivity at the border of electron localization and itinerancy. *Nat. Commun.* 4:2783 doi: 10.1038/ncomms3783 (2013).